Photocatalytic Degradation of the Light Sensitive Organic Dyes: Methylene Blue and Rose Bengal by Using Urea Derived g-C$_3$N$_4$/ZnO Nanocomposites

Fahad A. Alharthi *, Abdulaziz Ali Alghamdi, Hamdah S. Alanazi, Amjad Abdullah Alsyahi [ID] **and Naushad Ahmad**

Department of Chemistry, College of Science, King Saud University, Riyadh 11451, Saudi Arabia; aalghamdia@ksu.edu.sa (A.A.A.); hsenzi@ksu.edu.sa (H.S.A.); A.Alsyahi@hotmail.com (A.A.A.); anaushad@ksu.edu.sa (N.A.)

* Correspondence: fharthi@ksu.edu.sa

check for updates

Abstract: In this study, we report the fabrication of graphitic carbon nitride doped zinc oxide nanocomposites, g-C$_3$N$_4$/ZnO, (Zn-Us) by using different amount of urea. They were further characterized by X-ray Diffraction (XRD), Fourier-transform infrared spectroscopy (FT-IR), Raman, UV-vis, Scanning electron microscopy (SEM), and Transmission electron microscopy (TEM) techniques. The prepared nanocomposites were used as photocatalysts for the mineralization of the light sensitive dyes Methylene Blue (MB) and Rose Bengal (RB) under UV light irradiation, and corresponding photo-mechanism was proposed. Benefiting from these photocatalytic characteristics, urea derived g-C$_3$N$_4$/ZnO photocatalysts have been found to have excellent photodegradation activity against the MB and RB for 6 h and 4 h, respectively. Under the given experimental conditions, the degradation percentage of fabricated Zn-Us were shown ~90% for both model dyes. Compared to cationic MB dye, anionic RB dye is more actively degraded on the surface of prepared photocatalysts. The results obtained can be effectively used for future practical applications in wastewater treatment

Keywords: Rose Bengal; g-(C3N4); ZnO; Methylene Blue; UV-light; photocatalytic degradation

1. Introduction

Environmental and water pollution has become a great matter of concern with rapid industrialization, as pollutants are disposed into water bodies, having harmful effects on the environment. The dumped wastes which consist of mainly heavy metals, synthetic organic dyes, and pharmaceuticals, need to be treated effectively, especially synthetic organic dyes that are widely used in the printing, textile, cosmetic, and paper industries [1–3]. Photosensitive dyes with complex structures and long-lasting stability are highly toxic and can cause mutagenic and carcinogenic changes in humans and livestock [3]. Hence, the dumping of these dyes into water not only changes its colour but also regulates the oxygen levels, therefore, it is necessary to abate toxic dyes before dumping them into any water bodies. Various research has been done to overcome the problems associated with the decomposition of organic dyes and their removal from industrial wastewater by various processes such as thickening, adsorption, membrane filtration, and advanced oxidation processes [4,5]. Among them, the advanced oxidation process (AOP) has exposed superficial effectiveness in the direction of industrial wastewater treatment, particularly textile waste comprising synthetic dyes [6,7]. Such methods are embraced with various techniques such as photo-catalytic processes applied to vitiate organic pollutants and toxic chemicals prevailing in water bodies [8].

In recent years, the metal free polymeric visible light active graphitic carbon nitride (g-C$_3$N$_4$) analogue to graphite has attracted significant attention because of its suitable band alignment and

efficient redox potential for hydrogen evolution by its water splitting process, selective oxidation reactions in the presence of solar light, and the decomposition of organic waste pollutants and products [9–11]. g-C$_3$N$_4$ is a layered structure (interlayer distance of about 0.33 nm), with a large surface area, appropriate band gap energy (2.7 eV), and electron rich surface which is favored for its high photocatalytic performance [9–12]. Further, it has been considered as a favorable material with its elite physicochemical properties, such as inflexibility, light weight, stability, chemical inertness, water resistivity, and biocompatibility, which make it perfect for fabricating light emitting devices, sensing electrodes for hazardous chemicals, and photocatalysis process [11–14]. Interestingly, the matrix of g-C$_3$N$_4$ can offer active sites for binding with many organic/inorganic compounds or metals, which supply an appropriate route to functionalize g-C$_3$N$_4$ surface with relatively high reactivity [9,10,15,16]. Various kind of nitrogen and oxygen containing organic precursors such as urea, thiourea, cyanamide, dicyandiamide, and melamine are used for the fabrication of g-C$_3$N$_4$ by various strategies. However facile and simple the method is, on a large scale is still challenging because many staring materials are expensive, explosive, toxic, and environmentally hazardous. The most commonly inexpensive urea, N—O rich precursor, is used for its synthesis. Liu et al. prepared g-C$_3$N$_4$ on a large scale through the pyrolysis of urea by applying ambient pressure, high temperature, and different times intervals and used it as a photocatalyst for MB degradation using visible light [17]. Similar approach has been used for rhodamine B (RhB) dye by Dong and co-workers [18].

However, the photocatalytic studies of pure g-C$_3$N$_4$ are restricted owing to its high recombination rate of the electron hole pair, generated in the presence of light, and low effectivity in the visible light range [9–15,19,20]. Various approaches have been made to increase the photocatalytic performance of g-C$_3$N$_4$. Researchers have coupled g-C$_3$N$_4$ with many ultra and visible range inorganic semiconductors like ZnO, TiO$_2$, CdS, ZnWO$_4$, BiPO$_4$, Bi$_2$WO$_6$, and Ag$_2$O [21–23] to widen the separation between electron–hole pairs and consequently to trigger better photocatalytic performance through the coupling phenomenon. ZnO is an UV-light active type II semiconductor and its exciton binding energy and optical binding energy are 60 MeV and 3.37 eV, respectively, which limits the practical application in visible light photocatalysis [24]. The photo degradation of methyl orange and p-Nitrophenol using composite of g-C$_3$N$_4$–ZnO synthesized by calcination procedure with varying ZnO, as reported by Sun and co-workers [25], was found to be 3–6 times better in comparison with pure g-C$_3$N$_4$. Wang and co-workers also performed similar kinds of studies [26]. The production of core–shell nanoplates of N-doped ZnO/g-C$_3$N$_4$ via the ultrasonic dispersion process and their exceptional visible light photocatalytic activity has been reported by Kumar and co-workers, [24]. The deposition–precipitation technique has been used for the synthesis of g-C$_3$N$_4$/ZnO composite acting as visible light active photocatalyst by Liu and co-workers [27]. Wang and co-workers [28] reported the electrochemical synthesis of g-C$_3$N$_4$/ZnO nanotube and showed their enhanced photo electrochemical properties. All these reports reveal that a composite of ZnO and g-C$_3$N$_4$ gives an excellent photocatalytic activity under the illumination of solar light.

Methylene Blue (MB) is heterocyclic aromatic compound. It is a cationic dye widely used for dying cotton wool and silk. Rose Bengal (RB) is an anionic dye extensively used in dyeing and printing industries and is also used as an insecticide. These dyes could be dangerous if inhaled or come in contact with skin Thus, the removal of MB and RB from wastewater is a vital environmental problem.

Considering the above findings further gives us many opportunities to explore preparation methods that can influence the morphological, optical and photocatalytic performance. In this study we report the facile and single step fabrication of the g-C$_3$N$_4$/ZnO composite by the variation of urea. However, to the best of our understanding, there are still no reports on the preparation of g-C$_3$N$_4$ composites by the amount variation of urea without using additives. The low-cost urea is an active and stable precursor at high temperature, which is a suitable and economical approach for the large-scale production of g-C$_3$N$_4$ doped composites. The fabricated samples are characterized by several analytical techniques XRD, FTIR, Raman, UV-vis, SEM, and TEM and assessed in terms of their photocatalytic performance in the photocatalytic degradation of MB and RB as target pollutants in the presence of a UV

light. Under UV light illumination there was an immense improvement in the photocatalytic activity for the dissociation of MB and RB dyes. The present study reveals the mechanism for photocatalytic dye removal using g-C$_3$N$_4$/ZnO from aqueous solutions and the obtained results are compared with P25 and previously reported work.

2. Results and Discussion

2.1. X-ray Diffraction

The crystallinity of the powder samples was analyzed via XRD and the results are depicted in Figure 1. The two-diffraction peak at 2θ = 13.5 and 26.7 are observe in Zn-U2, indexed to the (100) and the (002) diffraction planes conforming to the JCPDS No. 87-1526 of the graphitic carbon nitride resemble the interplanar graphitic stacking plane of g-C$_3$N$_4$ [29]. In addition, Zn-U2 also shows the presence of some minor impurities along with g-C3N4 which remained during the polymerization and condensation processes of urea. These peaks are diminished in the other two nanocomposites. The sharp and strong diffraction peaks of ZnO are clearly supported the crystalline nature of the fabricated Zn-Us. In all samples, the diffraction peaks are identical in the two theta position, but their intensity decreases with the increasing the amount of urea in the order of Zn-U1 < Zn-U2 < Zn-U3. The various diffraction peaks for ZnO are observed at 2θ = 31.78°, 34.42°, 36.19°, 47.40°, 56.47°, 62.63°, 68.85°, and 76.71°, coinciding with (100), (002), (101), (102), (110), (103), (112), and (202) planes, respectively. These observed reflection planes represent the formation of the wurtzite (HCP) structure of ZnO and are well matched with JCPDS card no. 89-1397 [30]. The obtained results depict that the change in urea concentration in Zn-Us does not affect the configuration of ZnO nanoparticles. The XRD patterns of nanocomposites do not show any impurity peak which reveals the purity of the materials phase.
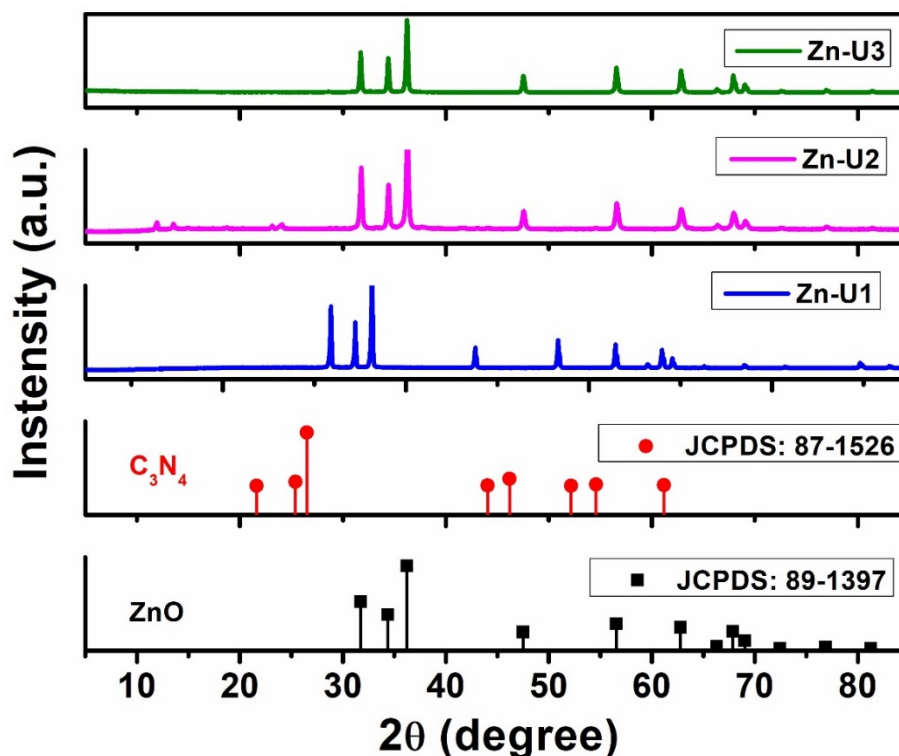

Figure 1. XRD patterns of the Zn-U1 Zn-U2 and Zn-U3 nanocomposites.

2.2. Fourier Transform Infrared Spectroscopy (FT-IR)

To check the purity of the fabricated products, FT-IR spectra were recorded and are shown in Figure 2. The broad stretching vibration band of internally/surface bonded O—H group of water is represented between 3500 cm^{-1} and 3200 cm^{-1} [31] which becomes broader with the decreasing amount of urea and indicates the degree of condensation or polymerization that is inversely increased. Various prime absorption bands from 1500 cm^{-1} to 1200 cm^{-1} can be nominated to the characteristic aromatic C–N, C=C, and C–C stretching bands of heterocycles and result from the extended C$_3$N$_4$ arrangement [32]. When increasing the urea concentration, the intensity of the observed peaks was found to decrease and prominent peak variations could be observed in the case of the Zn-U3 composite. This indicates that increasing the concentration the structure of g-C$_3$N$_4$ leads to partial deterioration. The bands located at 1550 cm^{-1} are related to the stretching vibration of C-N and C=N heterocycles [33,34]. Absorption peaks located at around 482 cm^{-1} are ascribed to the stretching vibration of Zn-O [35]. Zn-U1 and Zn-U2 show weak bending vibration around 820 cm-1, indicating the presence of ring of triazine while its absence in Zn-U3 indicates the complete polymerization in the case of Zn-U1 and Zn-U3. However, in the case of Zn-U2, it shows the presence of impurities which is in agreement with the XRD result. The other bands located from 1390 cm^{-1} and 1533 cm^{-1} might correspond to C-O vibration modes. The peaks found to be overlapped or completely disappeared for Zn-U3 nanocomposite may be due to the integration of g-C$_3$N$_4$ and ZnO [36], which is consistent with the XRD results. Thus, all these FTIR peaks confirmed the strong interaction between g-C$_3$N$_4$ and ZnO, and such a condition might play a vital role in promoting its activity as a photocatalyst [37].
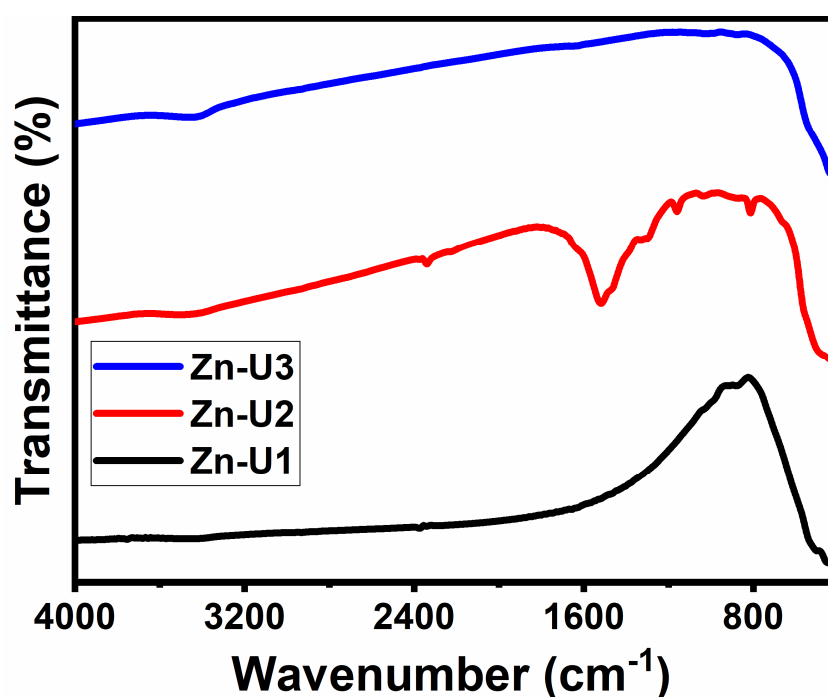

Figure 2. FTIR spectra of the Zn-U1, Zn-U2 and Zn-U3 nanocomposites.

2.3. Raman Spectroscopy

Structural defects and disorders of the synthesized samples were further investigated by Raman Spectroscopy. As shown in Figure 3, nine peaks are exhibited between 200 and 1200 cm^{-1} in the Zn-U1 sample. These bands were located at 275, 330, 379, 437, 510, 578, 645, 860, and 1157 cm^{-1}. However, the bands of g-C$_3$N$_4$ in nanocomposites are difficult to recognize in the Raman spectra due its high fluorescence properties and the weak intensities of the peaks. This reveals the weak scattering ability of g-C$_3$N$_4$ on the surface of the nanocomposites [38]. The band positioned at 437 cm^{-1}

corresponds to the Raman active and nonpolar optical E_2 mode of wurtzite hexagonal phase of ZnO, C_{6V}^4 (P6$_3$*mc*) space [39]. The Raman band located at 379 cm^{-1} corresponds to the infrared active A$_{1T}$ mode, ascribed the polar lattice bonds. The band appearing at 330 cm^{-1} are the qualified multi phonons mode (E$_{2H}$-E$_{2L}$) of ZnO [40]. The peak appearing at 578 cm^{-1} can be related to the infrared optically active E$_{1L}$ mode. The intensity of ZnO stretching vibration observed at 570 cm^{-1} are decreased in the order of Zn-U1 > Zn-U2 > Zn-U3 nanocomposite and almost disappear in the case of Zn-U3. The small peaks appearing at 275 cm^{-1}, 510 cm^{-1}, 645 cm^{-1}, 860 cm^{-1}, and 1157 cm^{-1} are characteristic of the g-C$_3$N$_4$ and agreed well with the reported literature [38,41–43]. Thus, the observed Raman scattering results confirmed that the synthesized sample is composed of g-C$_3$N$_4$ and ZnO and match well with the XRD results.
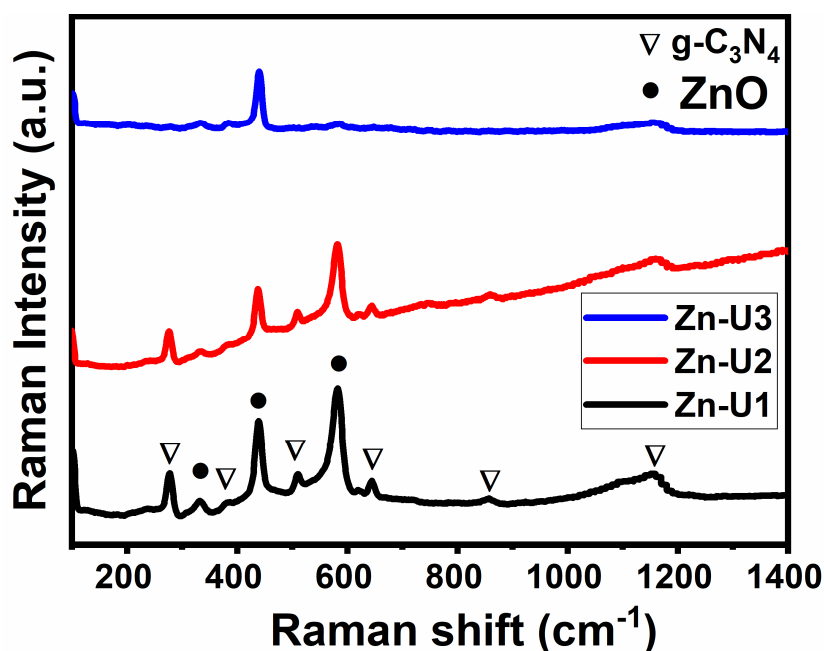

Figure 3. Raman spectra of the Zn-U1, Zn-U2, and Zn-U3 nanocomposites.

2.4. Morphological Study

In order to obtain the morphological information of the fabricated samples, the low and high magnified SEM images are presented in Figure 4. Figure 4a–f presents the SEM images of Zn-U1, Zn-U2, and Zn-U3 nanocomposites, respectively. It can be clearly seen that the surface morphology of fabricated nanocomposites contains a combination of triangular, semi-spherical, and disk-like nanocrystals of ZnO, which are anchored on the g-C$_3$N$_4$ nanosheets, confirming the formation nanocomposites of ZnO and g-C$_3$N$_4$. Interestingly, the morphology of Zn-U3 nanocomposites (Figure 4c,f) shows that the nanocrystals possess a porous structure, which possibly occurred due to the influence of released gases during the thermal polymerization reaction. In contrast, the morphology of Zn-U2 and Zn-U1 show only a moderate coverage of the g-C$_3$N$_4$ surface by ZnO nanocrystals. Moreover, as can be seen, the surface of Zn-U2 and Zn-U3 is rough compared to Zn-U1 which might be attributed to the stacking of nanosheets which provides reaction sites for photocatalytic reaction, and thus increases the chances of pollutants' interaction with photocatalysts. Thus, the fabricated nanocomposites materials are expected to play a vital role in determining its photocatalytic performances.
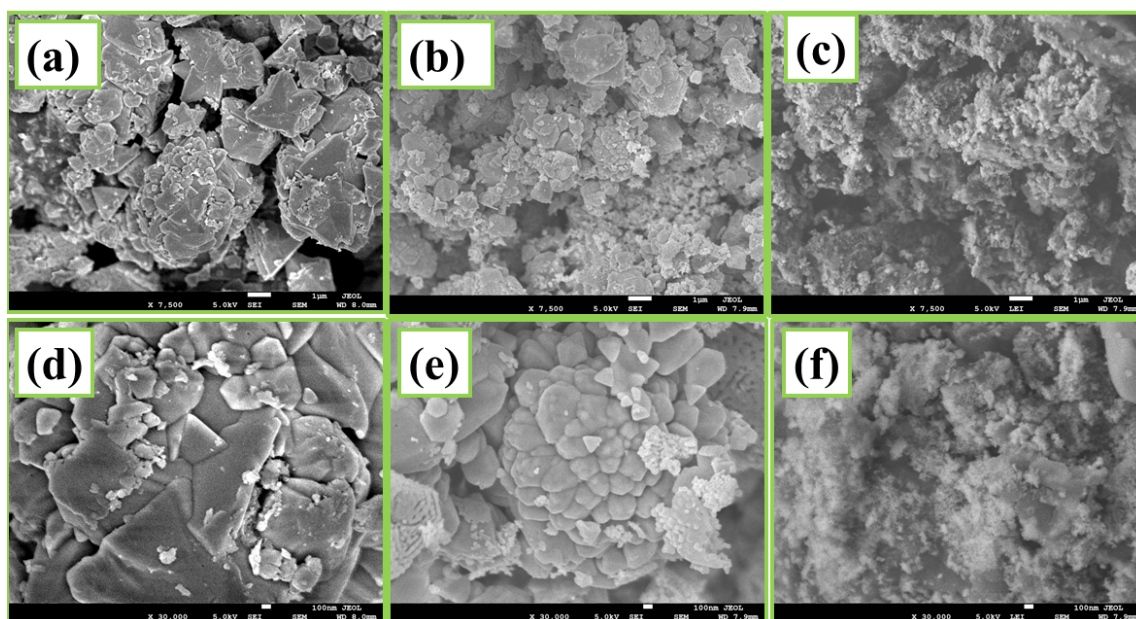
Figure 4. Low and high magnification SEM images of the Zn-U1 (**a**,**d**), Zn-U2 (**b**,**e**), and Zn-U3 (**c**,**f**) nanocomposites.

TEM analysis at different magnifications (low and high) was also performed to obtain more insight into the morphology of the nanocomposites. Figure 5a–d presents the TEM image of Zn-U1 and Zn-U3 nanocomposites, respectively. The TEM images show that the ZnO and g-C_3N_4 phases are simultaneously present and ZnO nanocrystal are anchored on the surface of g-C_3N_4 sheets. The obvious interaction between g-C_3N_4 and ZnO nanoparticles could facilitate the separation of photogenerated charge carriers and thereby enhance the photocatalytic activity of the photocatalysts. In the Zn-U3 nanocomposites, as shown in Figure 5c,d, ZnO nanoparticles as small dots are uniformly distributed on g-C_3N_4 nanosheets with a particle size ranging from 7 to 10 nm.

2.5. Textural Analysis (BET Surface Area)

For the comparison of the photocatalytic activity of prepared catalysts, the surface area, pore volumes, and pore size were determined by nitrogen isotherms. Isotherms are depicted in Figure 6 and the obtained results are summarized in Table 1. From Figure 6, its clear that the prepared samples have a mesoporous structure of type IV and categorically belong to H3 hysteresis loops [44]. It is also observed that the infection point shifted to lower relative pressure in the order of Zn-U3 > Zn-U2 > Zn-U1, demonstrating the contraction of the pore size distribution. From the Table 1, it can be seen that Zn-U3 has maximum surface area (S_{BET}) and pore volume which is one the favorable factor for its enhanced photocatalytic activity. It is also seen that pore volume increased and pore width decreased with urea concentration, i.e., Zn-U1 < Zn-U2 < Zn-U3.

Table 1. The surface properties of the catalysts were examined by BET surface area.

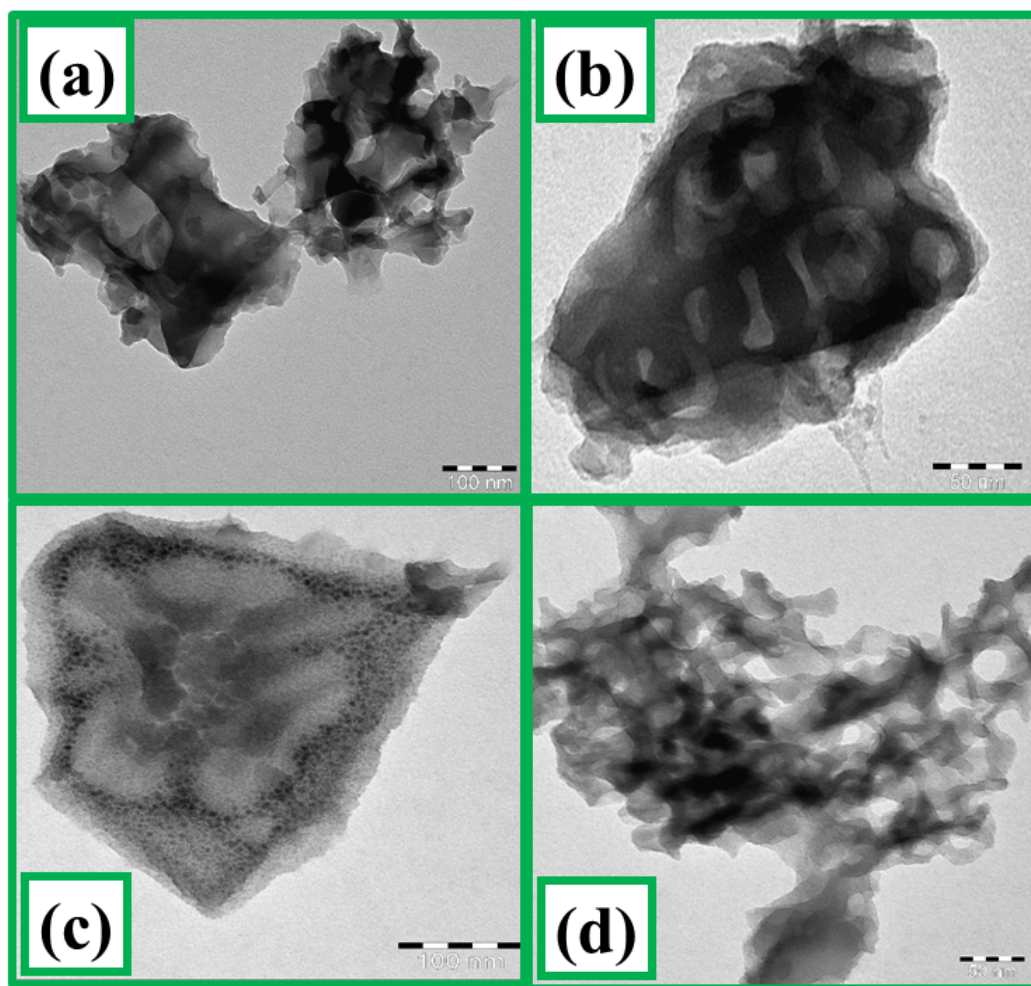| Sample	S_{BET} (m^2g^{-1})	Pore Volume (cm^3g^{-1})	Pore Size (nm)
Zn-U1	0.037	0.0005	169.9
Zn-U2	2.451	0.0224	53.5
Zn-U3	2.462	0.0155	43.0

Figure 5. Low and high magnification TEM images of the Zn-U1 (**a**,**b**) and Zn-U3 (**c**,**d**) nanocomposites.

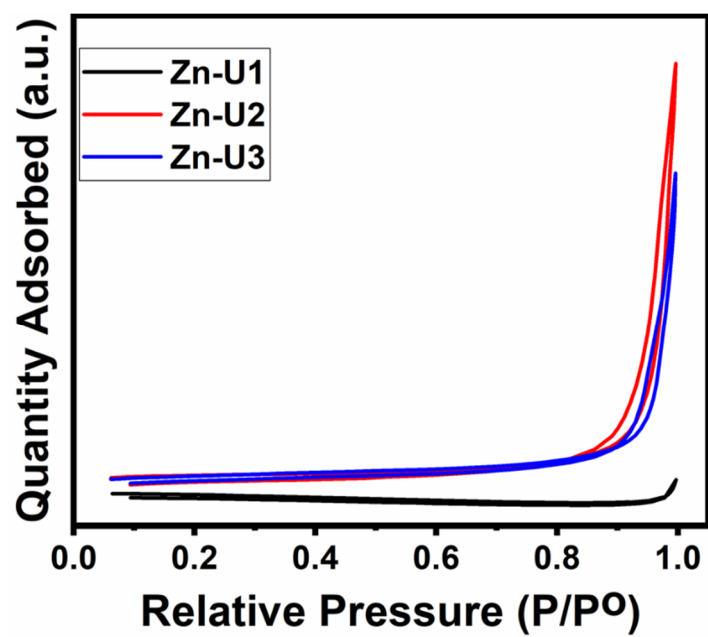**Figure 6.** N2-adsorbtion and desorption curves.

2.6. Photocatalytic Study

2.6.1. Photocatalytic Performance of Fabricated Nanocomposites

The degradation of the dyes (MB and RB) was conducted with photocatalytic experiments under the illumination of UV-light. The major peaks for MB (λ = 665 nm) and RB (λ = 546 nm) were used as the base of the photocatalytic reaction. Figures 7 and 8 display the time dependent photodegradation spectra of the model dyes under UV-light irradiation in the presence of photocatalysts and commercial pure TiO2 (P25). Figure 9a,b or Figure 10a,b represent the degradation efficiency and kinetic plots, respectively.
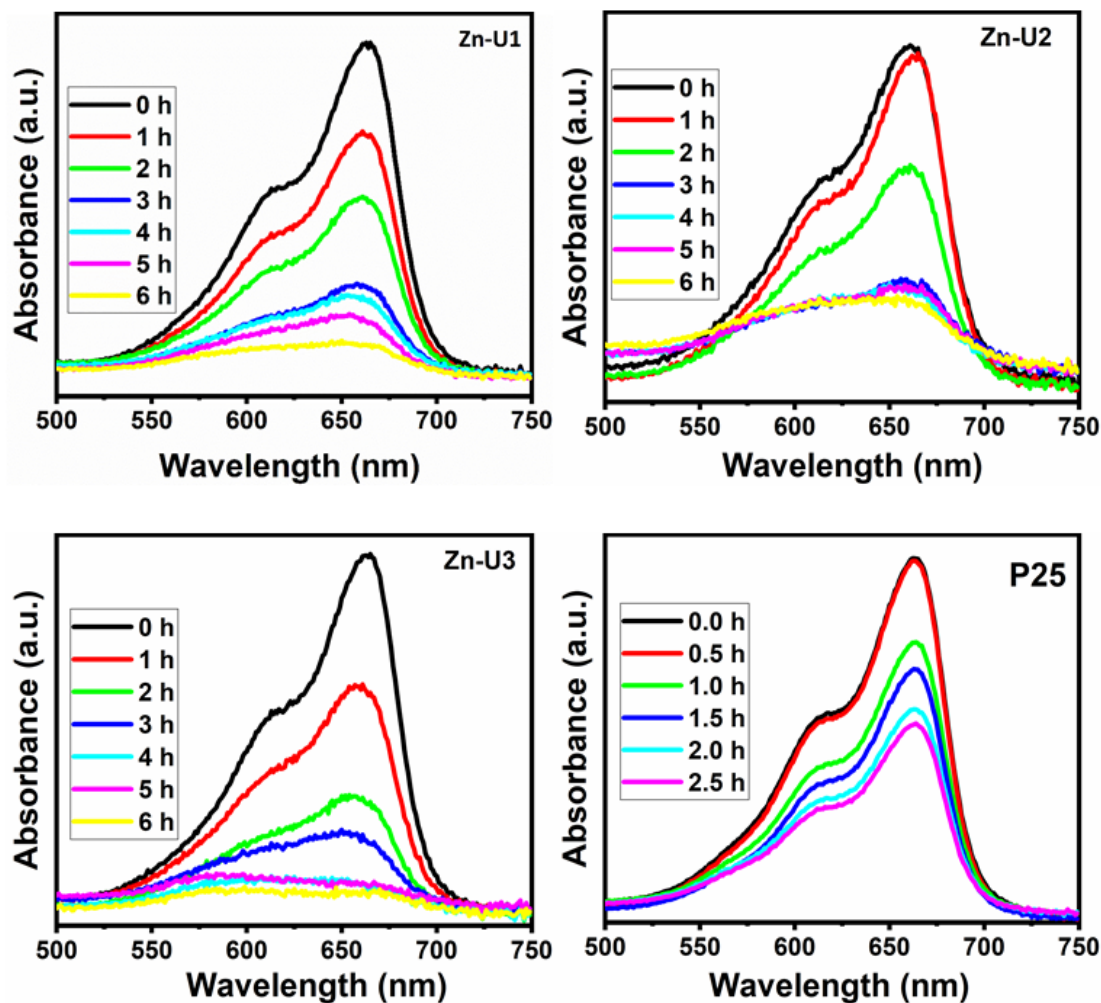
Figure 7. Time dependent spectral change of Methylene Blue (MB) solution catalyzed by Zn-U1, Zn-U2, Zn-U3 and P25 photocatalysts under UV-light irradiation.
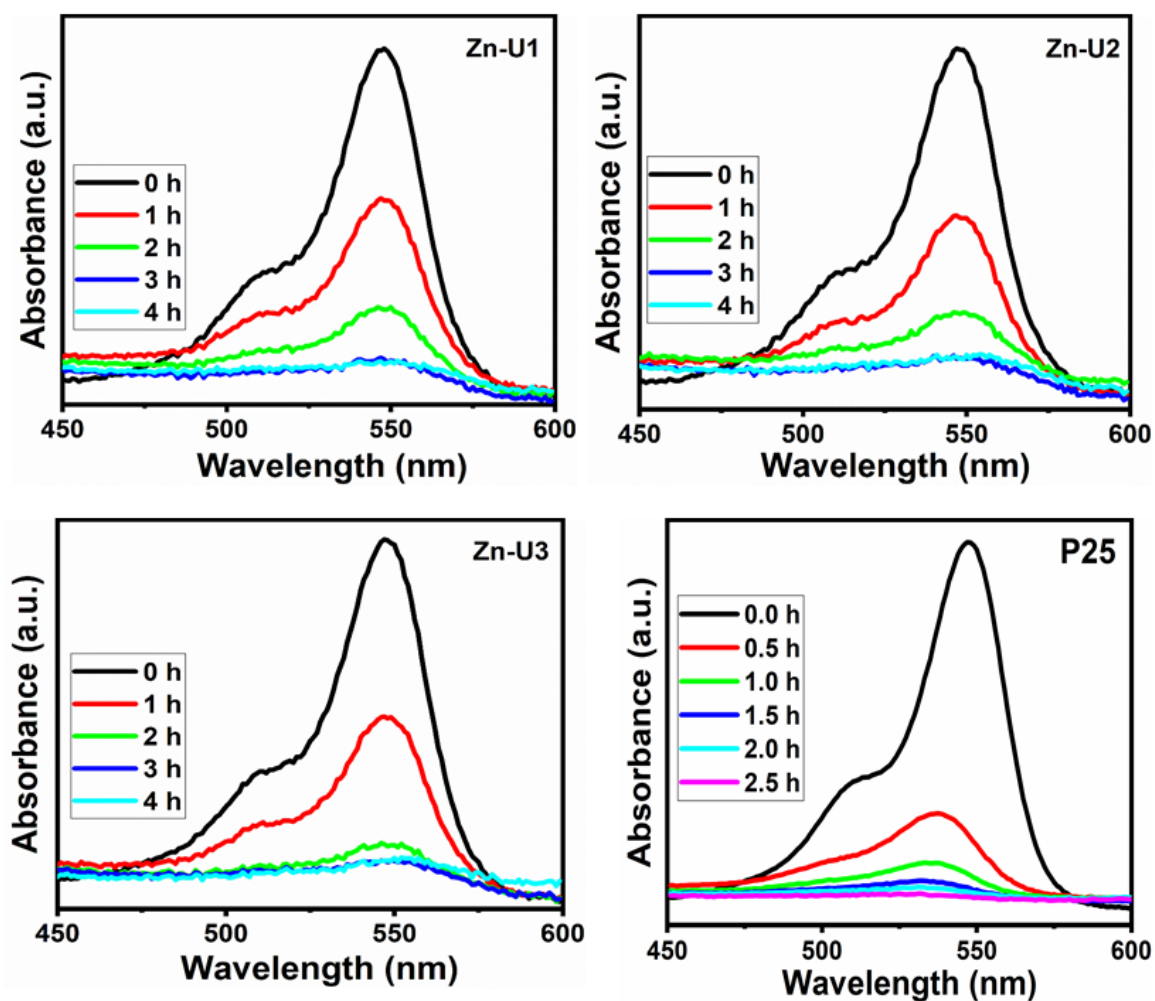
Figure 8. Time dependent spectral change of Rose Bengal (RB) solution catalyzed by Zn-U1, Zn-U2, Zn-U3, and P25 photocatalysts under UV-light irradiation.
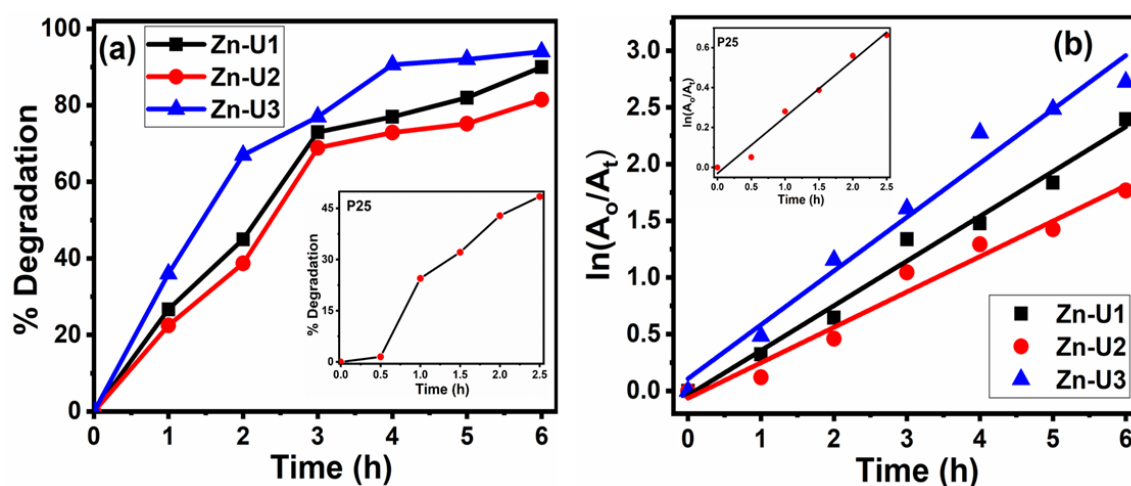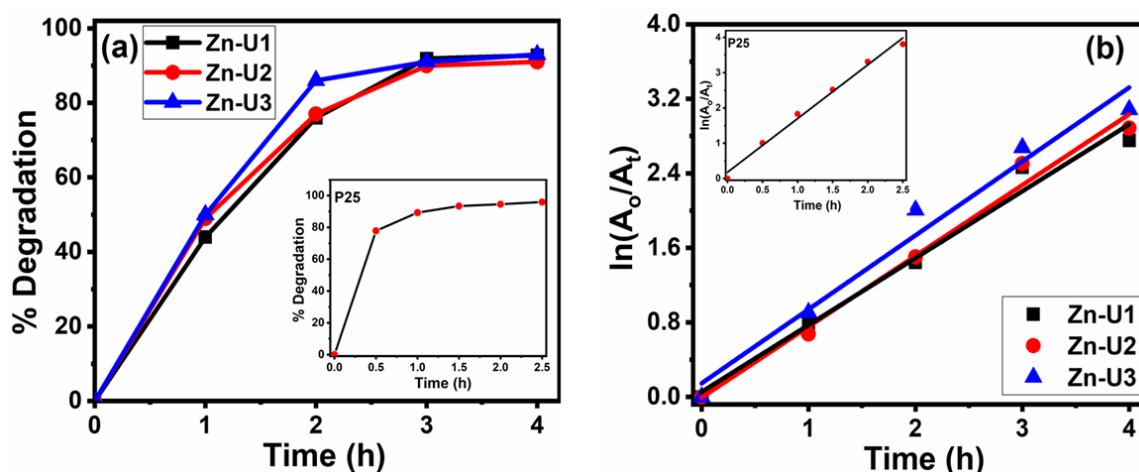

Figure 9. (**a**) MB dye degradation rate (**b**) the logarithmic change in concentration of MB as a function of irradiation time with insets of P25.

Figure 10. (**a**) RB dye degradation rate (**b**) the logarithmic change in concentration of RB as a function of irradiation time with insets of P25.

It can be observed that over ~80% of dyes are degraded after 6 h and 4 h irradiation of MB and RB, respectively, by fabricated nanocomposites and the maximum degradation of dyes was noticed in the case of Zn-U3. Due to the improved photocatalytic efficiency of the Zn-U3 nanocomposite, it facilitates the effective separation of photogenerated charge carriers [45]. In case of MB dye, the photocatalytic activity was found to be in the order of Zn-U3 > Zn-U1 > Zn-U2. This order shows that the Zn-U3 and Zn-U1composites express an enhanced degradation potential of 93.74% and 89.27%, respectively, as compared to Zn-U2 (80.78%). The decreased activity in the case of the Zn-U2 composite instead of having highest light absorption ability may be suppressing the transfer rate of the photo induced electron-hole pairs. The other reasons for the cause of decreased photoactivity of Zn-U2, may be that during the fabrication when two precursors, zinc nitrate and urea were mixed together, it was processed though the several steps such polymerization, condensation, heating, and thereafter annealed at a high temperature as stated, in the Materials and Method section of our manuscript. During these process different reaction intermediates were formed such as melamine, melam, melem, etc., as previously reported in the literature [30,46,47]. In our experiment we may assume that the peak notations in sample Zn-U2 shows the preliminary intermediate formation of these intermediate products which are in untraceable amounts and cannot determined well from the X-ray diffraction pattern. The data is also in accordance with the FTIR spectroscopy. At a higher temperature it seems from the peak intensities and its width (FWHM) in X-ray diffraction pattern that the material is highly crystalline in nature without any impurity of the other material. The FTIR also corresponds with the XRD and both are in agreement with the previously reported work. Similarly, the photoactivity potential for RB dye is in the order of Zn-U3 > Zn-U1 > Zn-U2. It can be observed that the rate of photodegradation of RB consumes less time as compared to MB, because its anionic nature creates a negative charge. Thus, the opposite charges on the RB dye and the catalyst enhance the efficiency of photocatalytic activity due the increase in their induced interaction. Additionally, the +Ve charged surface particle assists the migration of photo induced electrons and it could react with the adsorbed O_2 to produce $^{\bullet}O_2{}^{-}$. At the same time, the current process could also inhibit electron-hole recombination and generate more and more $^{\bullet}OH^{-}$ through reaction of the holes with the water. Therefore, both radical ions ($^{\bullet}O_2{}^{-}$, and $^{\bullet}OH^{-}$) could be responsible for the enhancement of the photocatalytic activity. Once the time of illumination increases, the interaction is also enhanced. Afterward, the photodegradation efficacy of photocatalysts was improved, which may be attributed to the dye molecule interaction with the surface of the photocatalysts [48].

It can be seen from the Figure 9b or Figure 10b the degradation process for both the dyes in the presence of catalysts follow pseudo first order kinetics. In the case of MB Zn-U3 showed the highest value for the reaction rate constant in comparison with Zn-U2 and Zn-U1. The rate constant of Zn-U3

(0.474 h^{-1}) is about 1.20 and 1.52 times greater than those of Zn-U1(0.394 h^{-1}), and Zn-U2 (0.312 h^{-1}), respectively. On the other hand, in the case of the rate constant values of RB dye, again Zn-U3 showed the highest value in comparison with Zn-U2 and Zn-U1. The rate constant of Zn-U3 (0.791 h^{-1}) is about 1.04 times and 1.10 greater than those of Zn-U1(0.761 h^{-1}), and Zn-U2 (0.718 h^{-1}), respectively. Thus, both the dyes confirm the higher photocatalytic activity. The rate constants and degradation efficiency of all samples along with TiO$_2$ (P25) evaluated for MB and RB are tabulated in Table 2. Moreover, the photocatalytic degradation properties of Zn-U3 has been compared with previously reported work in the terms of similar kinds of materials and dyes under the experimental operating conditions and the specific results such as degradation potential, rate constant, time, and irradiation source are mentioned in Table 3.

Table 2. Reaction rate constant and degradation efficiency of the dyes: Methylene Blue [a] and Rose Bengal [b].
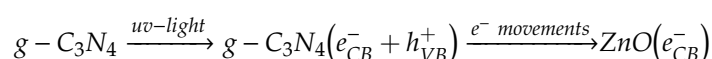
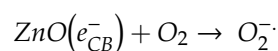| Sample	[a] Rate Constant (h^{-1})	[a] Degradation Efficiency (%)	[b] Rate Constant (h^{-1})	[b] Degradation Efficiency (%)
P25	0.282	47.87	1.522	95.62
Zn-U1	0.394	89.27	0.761	92.73
Zn-U2	0.312	80.78	0.718	90.57
Zn-U3	0.474	93.74	0.791	94.87

Table 3. Table showing comparison of photocatalysts and dyes with previously published works.

Sample	Dye	Time (h)	Light Source	DE(%)	Rate Constant	Refs
g-C$_3$N$_4$	MB	2	200 W Xe	62	0.0081 min^{-1}	[46]
GCN-Ag1	MB	2	200 W tungsten	96	0.0281 min^{-1}	[48]
3%Ag/g-C$_3$N$_4$	RhB	1.3	500 W Xe	98	0.0326 min^{-1}	[7]
ZnO/g-C$_3$N$_4$/Ag	MB	1	500 W tungsten	96	-	[49]
C$_3$N$_4$/Ag/ZnO/Zn plates	DO26	2	250 W Hg	94	-	[50]
Ag2S/g-C$_3$N$_4$/ZnO	MO	1.25	50 W Xe	75	-	[51]
g-C$_3$N$_4$-TiO$_2$	MB	2.6	200 W Xe	90	-	[52]
g-Fe$_2$O$_3$	RB	3.3	Visible	~100	0.0215 min^{-1}	[53]
Brookite TiO$_2$	RB	5	60 W fluorescent	98	-	[54]
a-Fe$_2$O$_3$	RB	2.3	200 W tungsten	98	0.0157 min^{-1}	[55]
g-C$_3$N$_4$-ZnO/HNTs	TC	1	350 W Xe	87	-	[56]
Zn-U3	MB	6	250 W Hg	95	0.474 h^{-1}	TW
Zn-U3	RB	4	250 W Hg	93	0.791 h^{-1}	TW

2.6.2. Proposed Mechanism

In this study, different frameworks of doped ZnO nanoparticles and negative surface charge of g-C$_3$N$_4$ increase the adsorption process of dye on its surface. The adequate photo-activity of Zn-Us nanocomposite can be elucidated on the basis of the alignment of the valence band (VB) and the conduction band (CB) positions of both g-C$_3$N$_4$ and ZnO distinctly. When UV-light falls over the fabricated nanocomposites, e$^-$ of the g-C$_3$N$_4$ are easily able to transport from the VB to CB (e$_{CB}^-$) and created h$^+$ on the VB (h$^+_{VB}$) of g-C$_3$N$_4$. The transported e$^-$ of the g-C$_3$N$_4$ are trapped by CB of ZnO for better separation between the e$^-$ h$^+$ pairs/delay the recombination. Now the electrons are easily available for the reaction with O$_2$ molecules and form a radical called superoxide radicals ($^\bullet$O$_2^-$) which further generate hydroxyl radicals ($^\bullet$OH) [24–26]. These •OH radicals are responsible for the mineralization of MB/RB. On the other hand, h$^+$ in VB of g-C$_3$N$_4$ is also responsible for the generation of $^\bullet$OH radicals from OH$^-$ ions, which are the active species in dye degradation [25,57]. The overall electronic transition and dye degradation reaction in g-C3N4/ZnO heterostructures are shown below:

$$g - C_3N_4 \xrightarrow{uv-light} g - C_3N_4\left(e_{CB}^- + h_{VB}^+\right) \xrightarrow{e^- \; movements} ZnO\left(e_{CB}^-\right)$$

$$ZnO\left(e_{CB}^{-}\right) + O_2 \rightarrow O_2^{-}\cdot$$

$$O_2^{-}\cdot + 2H^{+} \rightarrow 2\cdot OH$$

$$H^{+} + OH^{-} \rightarrow \cdot OH$$

$$\cdot OH + MB/RB \rightarrow Degradation\ products$$

It can be seen from the above reactions that the species like e^{-}, $^{\bullet}O_2^{-}$, $^{\bullet}OH$, and h^{+} are directly involved in the photocatalytic process. Also, the prepared g-C3N4/ZnO heterostructures due to the interfacial and synergetic process increase the electron transfer rate/current in turn the delayed recombination of photoinduced carriers. Thus, both the increased surface area and amount of urea in the case of the Zn-U3 sample can lead to better degradation efficiency towards the MB and RB dyes.

3. Experimental Section

3.1. Chemicals

Zinc nitrate hexahydrate ($Zn(NO_3)_2.7H_2O$, 99.999%) and urea (CH_4N_2O, Pur. > 99.0%) used in the experiments were supplied by Sigma-Aldrich-Germany. The organic dyes (Methylene blue and Rose Bengal) and other chemicals were of analytically pure grade and used without further purification. Deionized water was used throughout this study.

3.2. Synthesis of g-C_3N_4/ZnO Nanocomposites (Zn-Us)

The preparation of g-C_3N_4/ZnO photocatalysts was done by directly heating urea in a muffle furnace. Different amounts of urea (0.6, 1.2, and 1.8 gm) were dissolved completely in 10 mL of distilled water at 45 °C in a beaker. Later on, 0.259 mg of $Zn(NO_3)_2.6H_2O$ was added to the above solutions and stirred continuously. The suspension was then put into alumina crucible, enclosed tightly to avoid gas loss, and kept in muffle furnace at 600 °C for 1 h at the heating rate of 2 °C min^{-1}. The obtained calcined products were further characterized by sophisticated techniques and used as photocatalysts.

3.3. Characterization

The crystallinity of fine powders was recorded on Rigaku Ultimate 1 V X-ray diffractometer (Japan) with CuKα radiation source (λ = 1.5417 Å) in 2θ range of 10–80°. The Fourier transform infrared spectroscopy (FTIR) measurements were performed in the 400–4000 cm^{-1} range with KBr pellet method on Bruker Vertex 70 at room temperature. Raman spectra measurements of powdered sample were carried out on Raman spectrometer system (Renishaw In-Via) with a laser light irradiation of 785 nm. The surface area (S_{BET}) of fine powdered samples was performed with the aid of Tristar II plus 2.03 Micromeritics analyzer at liquid N2 temperature (77 K) and the pore volume and pore size was calculated by the BJH method. Prior to taking the measurements of the surface area, about 0.2 g Zn-Us photocatalysts were degassed at 200 °C for 2 h to get rid of impurities. The surface morphological aspects and particle size of fabricated catalysts were examined with scanning electron microscope (SEM) (JEOL JSM7600F, Japan) and their microstructures were examined with transmission electron microscope (TEM, JEOL 21000F, Japan), operated at an accelerating voltage of 80 kV.

3.4. Photocatalytic Activity Measurements

In this study, MB and RB was chosen as water pollutants and their degradation by the prepared photocatalysts were carried out on a photocatalytic reactor which consist of 250 W high-pressure Hg-lamp, applied as ultraviolet (uv) light source and 37 cm long quartz tube of 100 mL capacity. An aqueous solution (5 ppm) of the MB/RB and fabricated catalyst (10 mg) was photocatalyzed in a quartz reactor at RT under the UV light irradiation. The prepared suspension was sonicated in the dark for the dispersion and establishment of adsorption–desorption between the dye and the catalyst before irradiation. After that 2 mL centrifuged solution was taken out from reactor and its absorbance

was recorded at UV-Vis spectrophotometer at 546 nm for RB and 665 nm for MB, respectively, in the range of 200–800 nm for 6/4 h. The degradation rate was calculated using the following formula:

$$\text{Degradation rate} \ = \ \frac{A_o - A_t}{A_o} 100\% \tag{1}$$

where A_o and A_t refer to the initial absorbance and absorbance at time t of the dyes, respectively.

Furthermore, the rate constant for dye degradation process was estimated by Langmuir–Hinshewood equation:

$$ln\frac{A_o}{A_t} = kt \tag{2}$$

where t is degradation time (min) and k is the rate constant (min^{-1}).

4. Conclusions

In this work, Zn-Us nanocomposites were successfully synthesized by the deposition method and characterized by different techniques. The synthesized composite exhibited enhanced efficiency for photodegradation towards MB and RB dyes suggesting that the material can be a very promising multifunctional catalyst. The kinetics for photo-degradation was pseudo first order and about 90% degradation was achieved with the increasing concentration of catalyst after 6 h of exposure for MB dye and 4 h of exposure for RB dye, thus proving its potential application as a photocatalyst for wastewater treatment. Among the prepared materials, Zn-U3 showed highest apparent rate constant for both dyes. These results provide a clear insight which can be used in the future for other metals that can act as adaptable catalysts in the field of clean energy and environment.

References

1. Nas, M.S.; Calimli, M.H.; Burhan, H.; Yılmaz, M.; Mustafov, S.D.; Sen, F. Synthesis characterization, kinetics and adsorption properties of Pt-Co@GO nano-adsorbent for methylene blue removal in the aquatic mediums using ultrasonic process systems. *J. Mol. Liq.* **2019**, *296*, 112100. [CrossRef]
2. Senthil, R.A.; Osman, S.; Pan, J.; Khan, A.; Yang, V.; Kumar, T.R.; Sun, Y.; Lin, Y.; Liu, X.; Manikandan, A. One-pot preparation of AgBr/α-Ag2WO4 composite with superior photocatalytic activity under visible-light irradiation. *Colloids Surf. A* **2020**, *586*, 124079. [CrossRef]
3. Eghbali, P.; Hassani, A.; Sündü, B.; Metin, Ö. Strontium titanate nanocubes assembled on mesoporous graphitic carbon nitride (SrTiO3/mpg-C3N4): Preparation, characterization and catalytic performance. *J. Mol. Liq.* **2019**, *290*, 111208. [CrossRef]
4. Hassani, A.; Eghbali, P.; Ekicibil, A.; Metin, O. Monodisperse cobalt ferrite nanoparticles assembled on mesoporous graphitic carbon nitride (CoFe$_2$O$_4$/mpg-C3N4): A magnetically recoverable nanocomposite for the photocatalytic degradation of organic dyes. *J. Magn. Magn. Mater.* **2018**, *456*, 400–412. [CrossRef]
5. Alharthi, F.A.; Alghamdi, A.A.; Alothman, A.A.; Almarhoon, Z.M.; Alsulaiman, M.F.; Alzaqri, N. Green Synthesis of ZnO Nanostructures Using Salvadora Persica Leaf Extract: Applications for Photocatalytic Degradation of Methylene Blue Dye. *Crystals* **2020**, *10*, 441. [CrossRef]
6. Faraji, M.; Mohaghegh, N.; Abedini, A. Ternary composite of TiO2 nanotubes/Ti plates modified by g-C3N4 and SnO2 with enhanced photocatalytic activity for enhancing antibacterial and photocatalytic activity. *J. Photochem. Photobiol. B* **2018**, *178*, 124–132. [CrossRef]

7.　Qi, K.; Li, Y.; Xie, Y.; Liu, S.-Y.; Zheng, K.; Chen, Z.; Wang, R. Ag Loading Enhanced Photocatalytic Activity of g-C3N4 Porous Nanosheets for Decomposition of Organic Pollutants. *Front. Chem.* **2019**, *7*, 91. [CrossRef]

8.　Alharthi, F.A.; Alzaqri, N.; Marghany, A.E.; Alghamdi, A.A.; Alorabi, A.Q.; Baghdadi, N.; Alshehri, H.S.; Wahab, R.; Ahmad, N. Synthesis of nanocauliflower ZnO photocatalyst by potato waste and its photocatalytic efficiency against dye. *J. Mater. Sci. Mater. Electron.* **2020**, *31*, 11538–11547. [CrossRef]

9.　Ding, Z.; Chen, X.; Antonietti, M.; Wang, X. Synthesis of Transition Metal-Modified Carbon Nitride Polymers for Selective Hydrocarbon Oxidation. *ChemSusChem* **2011**, *4*, 274–281. [CrossRef]

10.　Wang, X.C.; Chen, X.F.; Thomas, A.; Fu, X.Z.; Antonietti, M. Metal-Containing Carbon Nitride Compounds: A New Functional Organic–Metal Hybrid Material. *Adv. Mater.* **2009**, *21*, 1609. [CrossRef]

11.　Yang, J.; Wu, X.; Li, X.; Liu, Y.; Gao, M.; Liu, X.; Kong, L.; Yang, S. Synthesis and characterization of nitrogen-rich carbon nitride nanobelts by pyrolysis of melamine. *Appl. Phys. A* **2011**, *105*, 161. [CrossRef]

12.　Iwano, Y.; Kittaka, T.; Tabuchi, H.; Soukawa, M.; Kunitsugu, S.; Takarabe, K.; Itoh, K. Study of Amorphous Carbon Nitride Films Aiming at White Light Emitting Devices. *Jpn. J. Appl. Phys.* **2008**, *47*, 7842. [CrossRef]

13.　Hong, J.; Xia, X.; Wang, Y.; Xu, R. Mesoporous carbon nitride with in situ sulfur doping for enhanced photocatalytic hydrogen evolution from water under visible light. *J. Mater. Chem.* **2012**, *22*, 15006–15012. [CrossRef]

14.　Li, Y.; Zhang, J.; Wang, Q.; Jin, Y.; Huang, D.; Cui, Q.; Zou, G. Nitrogen-Rich Carbon Nitride Hollow Vessels: Synthesis, Characterization, and Their Properties. *J. Phys. Chem. B* **2010**, *114*, 9429. [CrossRef]

15.　Wang, Y.; Li, H.; Yao, J.; Wang, X.C.; Antonietti, M. Synthesis of boron doped polymeric carbon nitride solids and their use as metal-free catalysts for aliphatic C–H bond oxidation. *Chem. Sci.* **2011**, *2*, 446–450. [CrossRef]

16.　Xu, J.; Zhang, L.; Shia, R.; Zhu, Y. Chemical exfoliation of graphitic carbon nitride for efficient heterogeneous photocatalysis. *J. Mater. Chem. A* **2013**, *1*, 14766–14772. [CrossRef]

17.　Liu, J.; Zhang, T.; Wang, Z.; Dawson, G.; Chen, W. Simple pyrolysis of urea into graphitic carbon nitride with recyclable adsorption and photocatalytic activity. *J. Mater. Chem.* **2011**, *21*, 14398–14401. [CrossRef]

18.　Dong, F.; Wu, L.; Sun, Y.; Fu, M.; Wu, Z.; Lee, S.C. Efficient synthesis of polymeric g-C3N4 layered materials as novel efficient visible light driven photocatalysts. *J. Mater. Chem.* **2011**, *21*, 15171–15174. [CrossRef]

19.　Takanabe, K.; Kamata, K.; Wang, X.; Antonietti, M.; Kubota, J.; Domen, K. Photocatalytic hydrogen evolution on dye-sensitized mesoporous carbon nitride photocatalyst with magnesium phthalocyanine. *Phys. Chem. Chem. Phys.* **2010**, *12*, 13020. [CrossRef]

20.　Yan, S.C.; Li, Z.S.; Zou, Z.G. Photodegradation of Rhodamine B and Methyl Orange over Boron-Doped g-C3N4 under Visible Light Irradiation. *Langmuir* **2010**, *26*, 3894–3901. [CrossRef]

21.　Zhang, Y.J.; Thomas, A.; Antonietti, M.; Wang, X.C. Activation of Carbon Nitride Solids by Protonation: Morphology Changes, Enhanced Ionic Conductivity, and Photoconduction Experiments. *J. Am. Chem. Soc.* **2009**, *131*, 50. [CrossRef] [PubMed]

22.　Wang, X.C.; Maeda, K.; Chen, X.F.; Takanabe, K.; Domen, K. Polymer Semiconductors for Artificial Photosynthesis: Hydrogen Evolution by Mesoporous Graphitic Carbon Nitride with Visible Light. *J. Am. Chem. Soc.* **2009**, *131*, 1680. [CrossRef] [PubMed]

23.　Yan, H.; Yang, H. TiO2–g-C3N4 composite materials for photocatalytic H2 evolution under visible light irradiation. *J. Alloys Compd.* **2011**, *509*, L26–L29. [CrossRef]

24.　Kumar, S.; Baruah, A.; Tonda, S.; Kumar, B.; Shanker, V.; Sreedhar, B. Cost-effective and eco-friendly synthesis of novel and stable N-doped ZnO/g-C3N4 core–shell nanoplates with excellent visible-light responsive photocatalysis. *Nanoscale* **2014**, *6*, 4830. [CrossRef]

25.　Sun, J.; Yuan, Y.; Qiu, L.; Jiang, X.; Xie, A.; Shen, Y.; Zhu, J. Fabrication of composite photocatalyst g-C3N4–ZnO and enhancement of photocatalytic activity under visible light. *Dalton Trans.* **2012**, *41*, 6756–6763. [CrossRef]

26.　Wang, Y.; Shi, R.; Lin, J.; Zhu, Y. Enhancement of photocurrent and photocatalytic activity of ZnO hybridized with graphite-like C3N4. *Energy Environ. Sci.* **2011**, *4*, 2922–2929. [CrossRef]

27.　Liu, W.; Wang, M.; Xu, C.; Chen, S. Facile synthesis of g-C3N4/ZnO composite with enhanced visible light photooxidation and photoreduction properties. *Chem. Eng. J.* **2012**, *209*, 386. [CrossRef]

28.　Wang, J.; Su, F.-Y.; Zhang, W.-D. Preparation and enhanced visible light photoelectrochemical activity of g-C3N4/ZnO nanotube arrays. *J. Solid State Electrochem.* **2014**, *18*, 2921–2929. [CrossRef]

29.　Bai, X.; Li, Y.; Xie, L.; Liu, X.; Zhan, S.; Hu, W. A novel Fe-free photo-electro-Fenton-like system for enhanced ciprofloxacin degradation: Bifunctional Z-scheme WO3/g-C3N4. *Environ. Sci. Nano* **2019**, *6*, 2850–2862. [CrossRef]

30. Fageria, P.; Gangopadhyay, S.; Pande, S. Synthesis of ZnO/Au and ZnO/Ag nanoparticles and their photocatalytic application using UV and visible ligh. *RSC Adv.* **2014**, *4*, 24962. [CrossRef]

31. Li, X.; Zhang, J.; Shen, L.; Ma, Y.; Lei, W.; Cui, Q.; Zou, G. Preparation and characterization of graphitic carbon nitride through pyrolysis of melamine. *Appl. Phys. A* **2008**, *94*, 387–392. [CrossRef]

32. Fang, H.-B.; Luo, Y.; Zheng, Y.-Z.; Ma, W.; Tao, X. Facile large-scale synthesis of urea-derived porous graphitic carbon nitride with extraordinary visible-light spectrum photodegradation. *Ind. Eng. Chem. Res.* **2016**, *55*, 4506–4514. [CrossRef]

33. Kumar, S.; Tonda, S.; Baruah, A.; Kumar, B.; Shanker, V. Synthesis of novel and stable g-C3N4/N-doped SrTiO3 hybrid nanocomposites with improved photocurrent and photocatalytic activity under visible light irradiation. *Dalton Trans.* **2014**, *43*, 16105–16114. [CrossRef] [PubMed]

34. Yan, S.C.; Li, Z.S.; Zou, Z.G. Photodegradation Performance of g-C3N4 Fabricated by Directly Heating Melamine. *Langmuir* **2009**, *25*, 10397–10401. [CrossRef]

35. Li, N.; Tian, Y.; Zhao, J.; Zhang, J.; Zuo, W.; Kong, L.; Cui, H. Z-scheme 2D/3D g-C3N4@ZnO with enhanced photocatalytic activity for cephalexin oxidation under solar light. *Chem. Eng. J.* **2018**, *352*, 412–422. [CrossRef]

36. Yin, J.; Chen, X.; Chen, Z. Quenched electrochemiluminescence sensor of ZnO@g-C3N4 modified glassy carbon electrode for fipronil determination. *Microchem. J.* **2019**, *145*, 295–300. [CrossRef]

37. Wu, C. Facile one-step synthesis of N-doped ZnO micropolyhedrons for efficient photocatalytic degradation of formaldehyde under visible-light irradiation. *Appl. Surf. Sci.* **2014**, *319*, 237–243. [CrossRef]

38. Yao, J.; Chen, H.; Jiang, F.; Jiao, Z.; Jin, M. Titanium dioxide and cadmium sulfide co-sensitized graphitic carbon nitride nanosheets composite photocatalysts with superior performance in phenol degradation under visible-light irradiation. *J. Colloid Interface Sci.* **2017**, *490*, 154–162. [CrossRef]

39. Kumar, G.M.; Ilanchezhiyan, P.; Kawakita, J.; Subramanian, M.; Jayavel, R. Magnetic and optical property studies on controlled low-temperature fabricated one dimensional cr doped ZnO nanorods. *CrystEngComm* **2010**, *12*, 1887–1892. [CrossRef]

40. Cusco, R.; Alarcon, E.L.; Ibanez, J.; Artus, L.; Jimenez, J.; Wang, B.; Callahan, M. Temperature dependence of Raman scattering in ZnO. *Phys. Rev.* **2007**, *B75*, 165202. [CrossRef]

41. Fan, C.; Miao, J.; Xu, G.; Liu, J.; Lv, J.; Wu, Y. Graphitic carbon nitride nanosheets obtained by liquid stripping as efficient photocatalysts under visible light. *RSC Adv.* **2017**, *7*, 37185–37193. [CrossRef]

42. Jiang, Z.; Zhu, C.; Wan, W.; Qian, K.; Xie, J. Constructing graphite-like carbon nitride modified hierarchical yolk–shell TiO2 spheres for water pollution treatment and hydrogen production. *J. Mater. Chem. A* **2016**, *4*, 1806–1818. [CrossRef]

43. Zhang, Y.; Pan, Q.; Chai, G.; Liang, M.; Dong, G.; Zhang, Q.; Qiu, J. Synthesis and luminescence mechanism of multicolor-emitting g-C3N4 nanopowders by low temperature thermal condensation of melamine. *Sci. Rep.* **2013**, *3*, 1943. [CrossRef] [PubMed]

44. Gregg, S.J.; Sing, K.S.W. *Adsorption, Surface Area, and Porosity*, 2nd ed.; Academic Press: London, UK, 1983.

45. Zheng, J.Y.; Haider, Z.; Van, T.K.; Pawar, A.U.; Kang, M.J.; Kim, C.W.; Kang, Y.S. Tuning of the crystal engineering and photo electrochemical properties of crystalline tungsten oxide for optoelectronic device applications. *CrystEngComm* **2015**, *17*, 6070–6093. [CrossRef]

46. Paul, D.R.; Sharma, R.; Nehra, S.P.; Sharma, A. Effect of calcination temperature, pH and catalyst loading on photodegradation efficiency of urea derived graphitic carbon nitride towards methylene blue dye solution. *RSC Adv.* **2019**, *9*, 15381. [CrossRef]

47. Paul, D.R.; Sharma, R.; Panchal, P.; Nehra, S.P.; Gupta, A.P.; Sharma, A. Synthesis, characterization and application of silver doped graphitic carbon nitride as photocatalyst towards visible light photocatalytic hydrogen evolution. *Int. J. Hydrog. Energy* **2020**, *45*, 23937. [CrossRef]

48. Neamtu, M.; Siminiceanu, I.; Yediber, A.; Kettrup, A. Kinetics of decolorization and mineralization of reactive azo dyes in aqueous solution by UV/H2O2 oxidation. *Dyes Pigments* **2002**, *53*, 93–99. [CrossRef]

49. Di, G.; Zhu, Z.; Zhang, H.; Zhu, J.; Qiu, Y.; Yin, D.; Küppers, S. Visible-light degradation of sulfonamides by Z-scheme ZnO/g-C3N4 heterojunctions with amorphous Fe2O3 as electron mediator. *J. Colloid Interface Sci.* **2019**, *538*, 256. [CrossRef]

50. Hassani, A.; Pari, M.F.; Eghbali, P. Facile fabrication of mpg-C3N4/Ag/ZnO nanowires/Zn photocatalyst plates for photodegradation of dye pollutant. *J. Photochem. Photobiol. A Chem.* **2020**, *400*, 112665. [CrossRef]

51. Feng, Y.; Wang, Y.; Li, M.; Lv, S.; Li, W.; Li, Z. Novel visible light induced Ag2S/g-C3N4/ ZnO nanoarrays heterojunction for efficient photocatalytic performance. *Appl. Surf. Sci.* **2018**, *462*, 896. [CrossRef]

52. Fu, D.; Han, G.; Liu, F.; Xiao, Y.; Wang, H.; Liu, R.; Liu, C. Visible-light enhancement of methylene blue photodegradation by graphitic carbon nitride-titania composites. *Mater. Sci. Semicond. Process.* **2014**, *27*, 966. [CrossRef]

53. Dutta, A.K.; Maji, S.K.; Adhikary, B. g-Fe$_2$O$_3$ nanoparticles: An easily recoverable effective photo-catalyst for the degradation of rose bengal and methylene blue dyes in the waste-water treatment plant. *Mater. Res. Bull.* **2014**, *49*, 28. [CrossRef]

54. Thuong, H.T.T.; Kim, C.T.T.; Quang, L.N.; Kosslick, H. Highly active brookite TiO$_2$-assisted photocatalytic degradation of dyes under the simulated solar−UVA radiation. *Prog. Natl. Sci. Mater. Int.* **2019**, *29*, 641. [CrossRef]

55. Maji, S.K.; Mukherjee, N.; Mondal, A.; Adhikary, B. Synthesis, characterization and photocatalytic activity of a-Fe$_2$O$_3$ nanoparticles. *Polyhedron* **2012**, *33*, 145. [CrossRef]

56. Li, J.; Zhou, M.; Ye, Z.; Wang, H.; Ma, C.; Huo, P.; Yan, Y. Enhanced photocatalytic activity of g-C$_3$N$_4$−ZnO/HNT composite heterostructure photocatalysts for degradation of tetracycline under visible light irradiation. *RSC Adv.* **2015**, *5*, 91177. [CrossRef]

57. Lin, X.; Guoa, X.; Shi, W.; Guo, F.; Zhai, H.; Yan, Y.; Wang, Q. Ag$_3$PO$_4$ quantum dots sensitized AgVO$_3$ nanowires: A novel Ag$_3$PO$_4$/AgVO$_3$ nanojunction with enhanced visible-light photocatalytic activity. *Catal. Commun.* **2015**, *66*, 67–72. [CrossRef]

Publisher's Note: MDPI stays neutral with regard to jurisdictional claims in published maps and institutional affiliations.